Author/s:
Balendhran, S;Taha, M;Wang, S;Yan, W;Higashitarumizu, N;Wen, D;Azar, NS;Bullock, J;Mulvaney, P;Javey, A;Crozier, KB

Title:
Flexible Vanadium Dioxide Photodetectors for Visible to Longwave Infrared Detection at Room Temperature

Date:
2023-10-13

Citation:
Balendhran, S., Taha, M., Wang, S., Yan, W., Higashitarumizu, N., Wen, D., Azar, N. S., Bullock, J., Mulvaney, P., Javey, A. & Crozier, K. B. (2023). Flexible Vanadium Dioxide Photodetectors for Visible to Longwave Infrared Detection at Room Temperature. Advanced Functional Materials, 33 (42), https://doi.org/10.1002/adfm.202301790.

Persistent Link:
https://hdl.handle.net/11343/338431

ADVANCED FUNCTIONAL MATERIALS
www.afm-journal.de

Flexible Vanadium Dioxide Photodetectors for Visible to Longwave Infrared Detection at Room Temperature

Sivacarendran Balendhran, Mohammad Taha, Shifan Wang, Wei Yan, Naoki Higashitarumizu, Dingchen Wen, Nima Sefidmooye Azar, James Bullock, Paul Mulvaney, Ali Javey, and Kenneth B. Crozier**

Flexible optoelectronics is a rapidly growing field, with a wide range of potential applications. From wearable sensors to bendable solar cells, curved displays, and curved focal plane arrays, the possibilities are endless. The criticality of flexible photodetectors for many of these applications is acknowledged, however, devices that are demonstrated thus far are limited in their spectral range. In this study, flexible photodetectors are demonstrated using a VO_x nanoparticle ink, with an extremely broad operating wavelength range of 0.4 to 20 µm. This ink is synthesized using a simple and scalable wet-chemical process. These photodetectors operate at room temperature and exhibit minimal variance in performance even when bent at angles of up to 100 ° at a bend radius of 6.4 mm. In addition, rigorous strain testing of 100 bend and release cycles revealed a photoresponse with a standard deviation of only 0.55%. This combination of mechanical flexibility, wide spectral response, and ease of fabrication makes these devices highly desirable for a wide range of applications, including low-cost wearable sensors and hyperspectral imaging systems.

1. Introduction

Flexible optoelectronics is an enabling technology for emerging platforms that include wearable sensors, curved displays, bendable solar cells, and curved focal plane arrays.[1–3] Most of these platforms require flexible photodetectors, i.e., devices that operate reliably under repeated mechanical strain or deformation, in contrast to conventional rigid devices. For some applications, such as sensing, mechanical flexibility of the device allows it to be used in a system that can conform to a certain shape, e.g. the human body. In other applications, mechanical flexibility allows the device to take a shape that is optimal for optical system performance. For the example, the image of an object formed using a simple lens lies on a curved surface known as the Petzval surface.[4–5] To enable high performance imaging to be achieved with conventional image sensors, which are arranged in flat focal plane arrays (FPAs), additional lens elements are needed to correct for the curvature and chromatic aberration.[6] This leads to compound lens systems that are bulky and have stringent tolerances, thereby increasing the manufacturing complexity. Natural evolution in biology, however, has created an alternative approach, in which the biological equivalent of the image sensor, i.e., the structures that detect the light, is a curved surface. An important example is human vision, where an image is formed on a curved retina. Our visual system can collect spectral, spatial and depth information, with a field of view of 135°.

S. Balendhran, N. S. Azar, K. B. Crozier
School of Physics
The University of Melbourne
Victoria 3010, Australia
E-mail: sbalendhran@unimelb.edu.au; kcrozier@unimelb.edu.au
M. Taha, S. Wang, W. Yan, J. Bullock, K. B. Crozier
Department of Electrical and Electronic Engineering
The University of Melbourne
Victoria 3010, Australia
The ORCID identification number(s) for the author(s) of this article can be found under https://doi.org/10.1002/adfm.202301790

DOI: 10.1002/adfm.202301790

N. Higashitarumizu, A. Javey
Electrical Engineering and Computer Sciences
University of California at Berkeley
Berkeley, CA 94 720, USA
N. Higashitarumizu, A. Javey
Materials Sciences Division
Lawrence Berkeley National Laboratory
California 94 720, USA
D. Wen, P. Mulvaney
School of Chemistry
The University of Melbourne
Victoria 3010, Australia
K. B. Crozier
ARC Centre of Excellence for Transformative Meta-Optical Systems
University of Melbourne
Victoria 3010, Australia

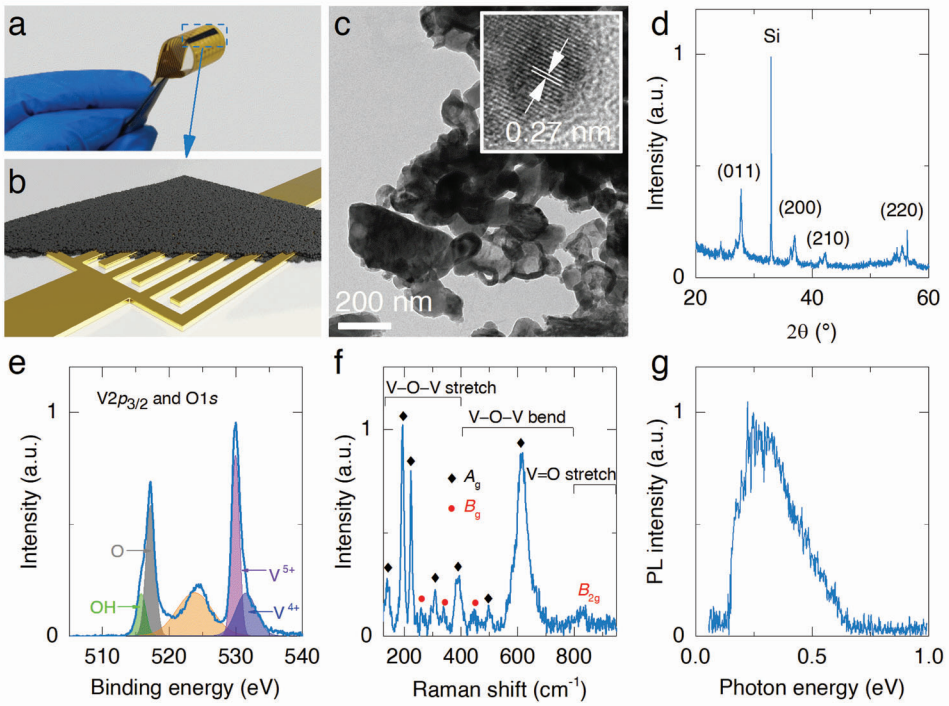

Figure 1. a) Photograph of flexible photodetectors. b) Schematic illustration of photodetector device architecture. c) TEM image of the VO_x nanoparticles. Inset shows a high-resolution TEM image showing the lattice spacing. d) X-ray diffraction, e) X-ray photoelectron, f) Raman, and g) normalized infrared photoluminescence spectra of the drop cast VO_x nanoparticles.

Arthropods have compound eyes providing a wide field of view of up to 360° and exceptional motion sensing capabilities. The success of curved biological image sensors has motivated researchers to produce concave FPAs, e.g. by emulating a concave surface using flat optoelectronic devices on flexible substrates and by developing perovskite nanowire based retinas.[7–8] Similarly, significant effort has been put into mimicking compound eyes by arranging silicon detectors in a convex FPA,[9] or using flat FPAs in combination with complex lenses structures to emulate ommatidia.[10–14] These approaches involve microelectromechanical structures, complex 3D fabrication processes, and/or will have limited spectral responsivity either due to the detectors or the optical components.

1D and 2D materials are viable alternatives for flexible photodetectors due to their exceptional mechanical flexibility and their self-terminating lattice structures.[15–19] Both solution processed and vapor deposition-based methods have been reported for visible to short-wave infrared detectors based on 1D and 2D materials.[20,21] Comprehensive reviews of flexible photodetectors based on various functional materials such as quantum dots, nanowires, 2D materials, organic semiconductors, perovskite materials are found in the literature.[1,22] These reviews note that narrow spectral response and slow response times are current challenges faced by flexible photodetectors. Some material platforms present opportunities to address these challenges. Graphene-based bolometers offer broad spectral responsivity and have the potential to be integrated into flexible platforms.[23–25] However, as graphene is a single atomic layer, it exhibits weak optical absorption and is challenging to produce over large areas and to integrate into flexible platforms.[16] Vanadium dioxide (VO_2) and silicon-based bolometers are used in longwave IR (LWIR) imaging applications, due to their high thermal coefficient of resistance at room temperature.[26,27] However, the existing synthesis and fabrication processes for these bolometers are not compatible with flexible platforms. Yttrium-barium-copper-oxide based microbolometers have been previously demonstrated on flexible substrates.[28] Nevertheless, these devices require encapsulation and back-reflectors to improve absorption which adds to the fabrication complexity, while their spectral range and performance under strain have not been reported. Organic material-based broad spectral photodetectors show promise;[27,29,30] however, these technologies are in their infancy and require further progress to be made on material stability and integration with CMOS electronics. Realizing flexible photodetectors with broad spectral responsivity (i.e., visible to longwave IR) using simple fabrication processes would enable cheaper, flexible photodetectors and truly curved focal plane arrays (i.e., both the substrate and detector elements are curved) that permit wide field-of-view imaging with simple lenses. This could enable low-cost sensing and detection capabilities that can be applicable in the biomedical, agriculture, space, and defense sectors.

In this work, we present flexible photodetectors covering the visible (400 nm) to longwave infrared (20 μm) spectral region that operate at room temperature. We demonstrate bend angles of up to 100° and bend radii down to 6.4 mm (**Figure 1**a). The devices show excellent stability when tested over more than 100 bend and release cycles, with negligible standard deviation in

photoresponse (0.55 %). The devices are fabricated using solution processed VO_x nanoparticles and adopting a simple interdigitated electrode architecture (Figure 1b), which can be easily integrated with CMOS processes. We characterize the material properties and the photodetector performance at room temperature. We then describe the mechanism governing the photoresponse. Finally, we present the performance of our photodetectors under tensile strain.

2. Results and Discussion

First, we characterize the as-synthesized material to quantify its composition. Figure 1c shows a transmission microscope (TEM) image of the drop cast VO_x nanoparticles. The typical diameter of the particles falls in the range of 100–150 nm. A high resolution TEM image of VO_x particles (Figure 1c, inset) shows a lattice spacing of 0.27 nm, indicating the presence of monoclinic vanadium dioxide (M1) in agreement with literature.[31,32] Next, we use x-ray diffraction (XRD) to assess the homogeneity of the crystalline structure across a large area drop cast film (Figure 1d). The peaks identified are in alignment with monoclinic VO_2 (JCPDS, No. 043–1051).[33,34] Of special note is the fact that the (011) plane is observed at $2\theta = 27.78°$, which validates that the material is a monoclinic (M1) structure across the assessed area.[34] We carry out x-ray photoelectron spectroscopy (XPS) to study the oxidation states and the composition of the film. The spectrum plotted as Figure 1e shows the presence of V^{4+} and V^{5+} peaks. The existence of V^{5+} is due to the rapid surface oxidation of VO_2 and is commonly seen in non-passivated VO_x films.[31,32] At the O1*s* peak, a shoulder corresponding to OH is also seen, due to adsorption of moisture on the surface. Figure 1f plots the Raman spectrum of the VO_x film. Raman peaks are observed at 138.9, 193.3, 222.3, 308.7, 337.3, 388.4, 617.4, and 821.9 cm^{-1}. These peaks are consistent with monoclinic VO_2.[32,35] Collectively, these results indicate that the drop-cast films are predominantly composed of monoclinic VO_2 with a native V_2O_5 surface oxide. Hence, we refer to the material as VO_x. Next, we characterize the infrared photoluminescence of the material at room temperature and plot it as Figure 1g. We observe broad spectral PL in the range of 0.15–0.6 eV, with a peak at 0.25 eV. The bandgap of monoclinic VO_2 (M1) is reported to be 0.6 eV and rutile VO_2 (R) behaves as a semimetal.[36] However, during the insulator to metal transition (IMT) in VO_2, pseudo gap states are observed that exhibit optically induced electronic transitions in the mid-infrared.[37] The broad IR PL observed here can be attributed to this same phenomenon, where IMT is induced by the incident photon energy, leading to these pseudo-gap states. Although IR PL indicates a bandgap in the MWIR range, we demonstrate a long-wave infrared response well below the bandgap of VO_x, which we attribute to a photothermal bolometric effect.

To characterize the photodetector performance, we use a mid-wave infrared laser ($\lambda = 2.2$ µm) as an illumination source. Refer to the Experimental Section for detailed information. First, we characterize the device response time to optical pulses, using an external square wave as a trigger for the laser diode (illumination intensity 2.55 mW mm^{-2}). The normalized photoresponse versus time is plotted as **Figure 2**a. At a bias of 145 mV, we find the rise and fall times to be 712 and 240 ms, respectively. We estimate the −3 dB roll-off point to be 0.5 Hz, based on the relationship $f_{-3\,dB} = 0.35/t_R$, where t_R is the rise time. The measured photoresponse to an optical pulse train is observed to show no baseline drift (Figure S1a, Supporting Information). Next, we study the current-voltage (*I*–*V*) characteristics of our devices. An *I*–*V* curve of a representative device under dark conditions and its bias dependent photocurrent under illumination ($\lambda = 2.2$ µm, 0.26 mWmm^{-2}) are presented as Figure 2b. Refer to Figure S1b (Supporting Information) for these curves plotted in a linear scale. The *I*–*V* characteristics of the device shows a linear behavior below 0.3 V and a subtle super linear behavior between 0.3 – 1 V (Figure S1b, Supporting Information), under dark and illumination conditions. These originate from the properties of the VO_x/Au interface. Using these results, we plot the photoresponsivity versus bias voltage as Figure 2c. The responsivity is also observed to be linear up to a bias of 0.3 V ($R \propto V^{1}$) and super linear between 0.3 to 1 V ($R \propto V^{1.6}$). The 2D correlation coefficient between the dark *I*–*V* characteristics and responsivity versus voltage characteristics is calculated to be unity. Since the responsivity of a bolometer follows the thermal coefficient of resistance (TCR), a photoinduced resistance change is measured as the photocurrent. A perfect 2D correlation indicates that the responsivity as a function of voltage in our devices is governed by the VO_x/Au contact interface, further suggesting it is a bolometric effect. We calculate the normalized photocurrent to dark current ratio (NPDR), defined as the ratio between the responsivity and dark current (Figure S1c, Supporting Information). Within the linear regime (i.e., below 0.3 V bias), on average, NPDR remains constant (256 W^{-1}). For bias voltages above 0.3 V, it is observed to increase up to a value of 346 W^{-1} at 1 V. We therefore operate our devices in the linear regime below 0.3 V, at a dark current value of 0.2 mA. Next, we characterize the incident power dependence of the photocurrent and responsivity. Figure 2d presents photocurrent versus incident power density. The photocurrent increases linearly with power density ($I_{Ph} \propto P^{1}$) over the range 0.2 to ≈5 mW mm^{-2}. For power densities greater than 5 mW mm^{-2}, a non-linear behavior ($I_{Ph} \propto P^{3.2}$) is observed. Consequently, in the linear regime (<5 mW mm^{-2}), the responsivity and detectivity (D^*) are observed to be constant (on average 70 mA W^{-1} and 1.17×10^6 cmHz$^{0.5}$W^{-1}, respectively). A dramatic increase in responsivity is observed beyond 5 mW mm^{-2}, reaching 268 mAW^{-1} with a peak D^* of 4.47×10^6 cmHz$^{0.5}$W^{-1}. We attribute this non-linear bolometric response to the photoinduced insulator to metal transition in VO_x, which will be discussed later. Finally, we characterize photoresponsivity as a function of wavelength, to determine the spectral bandwidth of our devices. As seen in Figure 2f, our devices show an ultra-broad spectral responsivity from 0.4 to 20 µm. We attribute this to a photothermal bolometric response, induced by the broad spectral absorption of our device (Figure S2, Supporting Information). In the visible to SWIR range, steady-state responsivity is measured to be relatively flat. We expect to a simlar behavior across the MWIR to LWIR range, however, the responsivity increases with wavelength. We attribute this effect to the limitation of the measurement technique, where the slowest modulation frequency of the source is beyond the bandwidth of our device. This results in the device acting a low-pass filter and underestimating the photoresponse at high frequencies (MWIR range). The roll-off of this filter effect is observed as the gradient in responsivity. We characterize a commercial deuterated triglycine sulfate (DTGS) detector

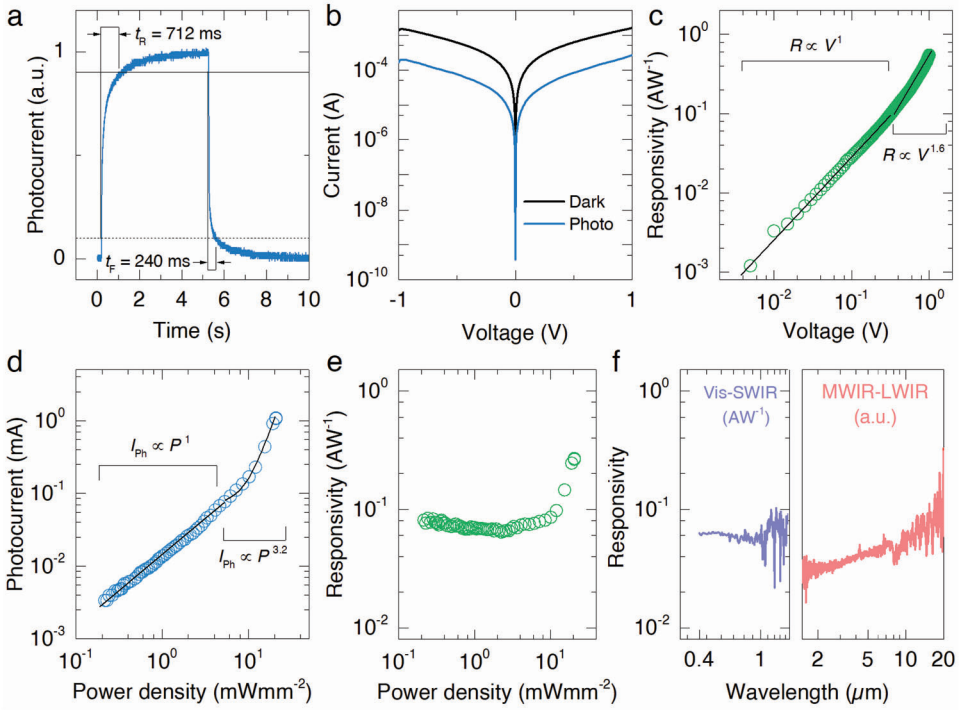

Figure 2. Photodetector characterization at $\lambda = 2.2$ µm. a) Normalized photoresponse to pulsed illumination, indicating the rise and fall times (10% – 90%). b) Current-voltage characteristics under dark and illumination conditions. c) Responsivity versus bias voltage. d) Photocurrent and e) responsivity as a function of illumination power density, characterized under chopped illumination. f) Responsivity versus wavelength across visible to SWIR (left panel, AW^{-1}) and MWIR to LWIR (a.u.). The devices are biased between 100–145 mV, to achieve a fixed dark current of 0.2 mA.

beyond its bandwidth and make the same observations (Figure S3, Supporting Information). Refer to the Experimental Section for details on the responsivity characterization. We also compare our work with other reported photodetectors with broad spectral response that operate at room temperature (Table S1, Supporting Information). Our work ranks as one of the top reports on broad spectral responsivity with the added benefit of being on a flexible platform.

Vanadium dioxide has been extensively used for bolometer applications in the longwave infrared range (6–14 µm).[38,39] We too attribute the broad spectral responsivity of our devices to a bolometric effect, since the responsivity is dependent on the incident power density and remains relatively constant across a broad spectral range. To confirm that the behavior of our device is governed by the bolometric effect, we characterize the effect of temperature on its performance. To do so, we fabricate a detector on a polyimide/SiO_2/Si substrate. The fabrication processes and the detector dimensions are identical to our flexible detectors, except that the polyimide layer is attached to an SiO_2/Si chip and packaged into a 28-pin chip carrier. This makes the device compatible with a cryostat for temperature-dependent resistance and photoresponse characterization. We measure the *I*–*V* characteristics of the detector as a function of temperature (**Figure 3**a) under dark conditions. It can be seen from Figure 3a that the *I*–*V* curves are approximately linear, and increase in slope (i.e., exhibit lower resistance) as temperature increases. In Figure 3b (left axis), we plot resistance versus temperature, which exhibits a non-linear behavior. Using this data, we calculate the temperature coefficient of resistance (α):[40]

$$\alpha = \frac{1}{R}\frac{\partial R}{\partial T} \times 100 \quad (1)$$

where R is the bolometer channel resistance and T is the absolute temperature. We plot the measured α versus T as Figure 3b (right *y*-axis). Our devices show room temperature α of 2–3 %K^{-1}, which is comparable to values reported in literature,[41,42] where the VO_x bolometers are fabricated using physical vapor deposition techniques on membranes. A steady increase in α is seen till 330 K, beyond which a sharp rise is observed peaking at 347 K, at which α = 9.5 %K^{-1}. A similar behavior in α of VO_x, at the temperature induced insulator to metal transition (IMT) point is reported in the literature.[40]

Next, we measure the photocurrent (at λ = 2.2 µm) as a function of temperature and incident power density and plot as Figure 3c. At room temperature, the photocurrent follows a similar trend to that seen in Figure 2d. However, as the temperature is increased, we observe a saturation point in the detector, beyond which we have $I_{Ph} \propto P^{0.7}$. With increasing temperature, this saturation point shifts toward lower incident power densities. We also characterize the responsivity as a function of temperature and incident power density, with the room temperature results matching the trend that seen in Figure 2e. The fact that the photocurrent saturates means that each responsivity versus incident power density curve (measured at a given temperature) exhibits a peak at a certain incident power density. These

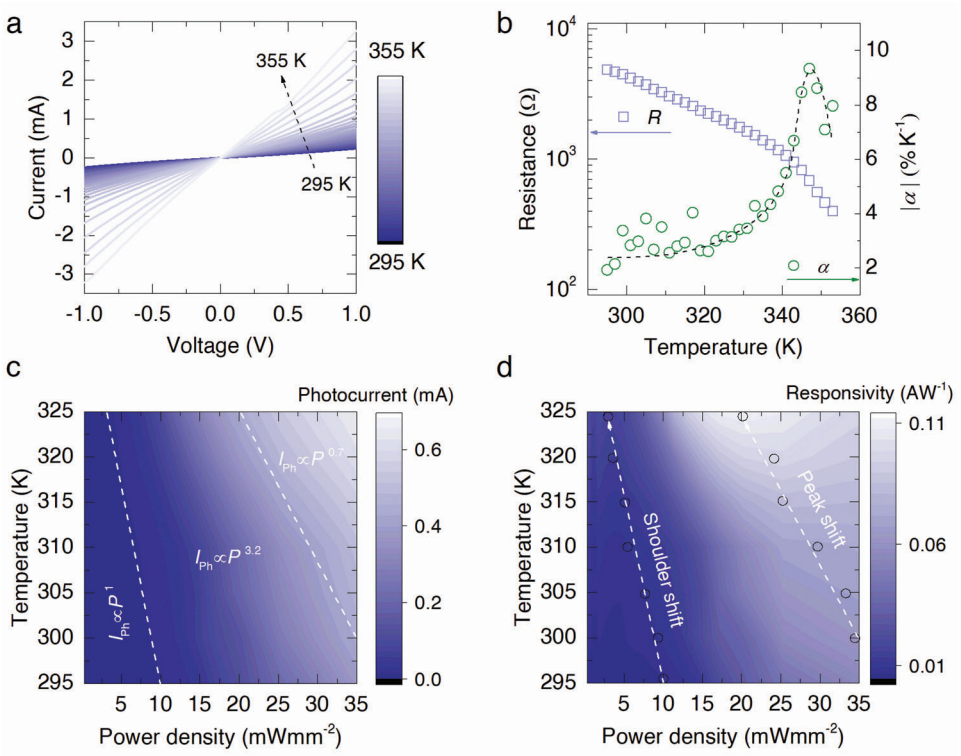

Figure 3. Temperature dependence of a) Temperature dependence of *I–V* characteristics. b) Resistance and temperature coefficient of resistance versus temperature, measured at a bias of 0.4 V. Black dashed line is a trend line. Temperature and incident power density dependence of c) photocurrent and d) responsivity, at $\lambda = 2.2$ µm. Photodetector is biased at 0.4 V.

peaks occur at lower incident power densities with increasing temperature. Log-log scale plots of the photocurrent and responsivity are presented as Figure S2 (Supporting Information) for comparison. The trend in responsivity versus incident power density (Figure 3d; Figure S2b, Supporting Information) is similar to the trend in α versus temperature observed at IMT (Figure 3b). This suggests that the responsivity of our detector is proportional to α, and that the non-linear behavior of the responsivity is due to a photoinduced IMT of the VO_x film. At low incident power densities, the change in resistance (and therefore the photocurrent) is approximately proportional to power density. However, at a threshold of ≈5 mW mm^{-2}, photoinduced IMT of VO_x is triggered. At power densities beyond this threshold, responsivity dramatically increases and reaches a peak. This is consistent with the α versus temperature curve (Figure 3b), where α is observed to dramatically increase and peak at IMT. As the detector temperature is increased, this photoinduced IMT threshold and the peak responsivity shift to lower incident power densities (Figures 3d and 2b). Similar observations are made concerning responsivity versus incident power density across the Vis-NIR spectral range (Figure S5, Supporting Information). Furthermore, the responsivity at a given incident power density is observed to remain relatively constant across this spectral range, independent of wavelength (Figure S5b, Supporting Information). Collectively, these results confirm that the mechanism governing the photoresponse is a bolometric effect and that non-linear behavior in responsivity versus power density is due to photoinduced IMT. The results also show that by precisely controlling the detector temperature, we can operate the detectors at or below the VO_x IMT threshold. By operating the detectors at the IMT temperature, the non-linear high responsivity region can be leveraged for detecting low-intensity light.

Next, we characterize the performance of our photodetectors under tensile strain, by bending the devices using a home-built uniaxial strain stage and comparing the measured photoresponse to that of the device under no strain. Refer to the Experimental Section for a detailed description of the setup. A schematic illustrating the device under strain is presented as **Figure 4**a. By reducing the distance (d) between the end terminals of the flexible printed circuit, we achieve bend angles (θ) of up to 100°. Refer to Video S1 (Supporting Information) for an animated video of the experiment. At each step, we measure the corresponding bend radius from a photograph of the device using image processing and plot it as a function of bend angle (Figure 4b). The smallest bend radius achieved using this setup is 6.4 mm at a bend angle of 99.4°. We estimate the device strain (ε) using the following equation:[43]

$$\varepsilon = \frac{t}{2r} \times 100 \quad (2)$$

where t is the thickness of substrate and r is the bend radius. Here, the uniaxial strain is proportional to the substrate thickness. As we aim to produce a device that can be bent without compromising the detector performance, we choose the substrate thickness (50 µm) to minimize the device strain. The

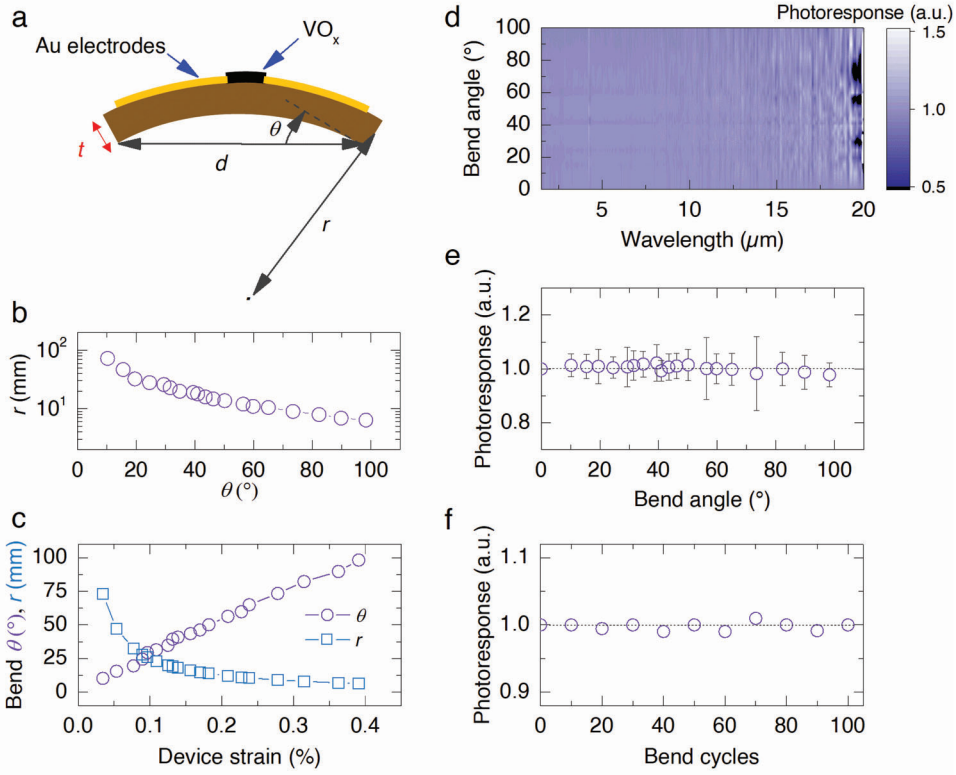

Figure 4. Photodetector characterization under tensile strain. a) Schematic illustration of device under tensile strain, showing bend radius (r), bend angle (θ) and the distance (d) between the device terminals. b) Experimentally achieved bend r versus θ, upon varying d from 5 cm (no strain) to 1 cm (highest % strain). c) Calculated tensile strain as a function of experimentally achieved r and θ. d) Photoresponse versus wavelength and bend angle, normalized to the photoresponse under no strain. e) Normalized photo response averaged between $\lambda = 1.5$–19 μm and presented as function of bend angle. Error bars indicate the standard deviation (γ-error $= 2\sigma$). f) Normalized photoresponse versus number of bend cycles.

estimated device strain versus bend angle and radius are plotted as Figure 4c. The maximum device strain achieved in this setup is 0.4%, at θ ~100°. We measure the photoresponse spectra at various bend angles and normalize to the spectrum measured at 0° (Figure 4d). It is seen that the variation in photoresponse with θ is negligible. Large variations in the normalized photoresponse (≈50%) seen near $\lambda = 20$ μm are attributed to low source power density at this wavelength, which results in the signal to noise ratio approaching unity. Refer to Figure S6 (Supporting Information) for a comparison of the raw photoresponse spectra at bend angles between 0° – 100°, the source power spectrum, and the measurement noise floor. To quantify the stability of the devices, we average the photoresponse over the measured wavelength range and plot it as a function of bend angle, with the standard deviation plotted as error bars (Figure 4e). On average, the normalized photoresponse for bend angles from 0° to 100° shows a standard deviation of less than 1.1%. Next, we characterize the cyclic endurance of our detectors by subjecting them to 100 cycles of bend and release test at θ ~100°. We measure the photoresponse at every 10^{th} cycle and normalize the results to the initial measurement (Figure 4f). The normalized photoresponse shows a standard deviation of just 0.55% over 100 bend and release cycles. We also do not observe any notable variations in the photoresponse time and the current noise density of the detectors (Figures S7 and S8, Supporting Information), suggesting that the VO_x films or the contacts do not deteriorate under bend angles of up to 100°. Collectively, these results indicate that our detectors are robust and can be used for flexible photodetection over a broad spectral region.

3. Conclusion

In conclusion, we have successfully developed a new device: flexible photodetectors based on VO_x nanoparticle ink. These photodetectors boast an impressive operating wavelength range, from the visible to the long wave infrared, with room-temperature performance. On average, we demonstrate responsivities of 70 mA W^{-1}, which can be increased up to 268 mA W^{-1}, during the IMT of VO_x, with a specific detectivity on the order of 10^6 Jones. Not only do they withstand significant bending, but they also maintain their photoresponse with minimal standard deviation (0.55%) even under repeated bending and releasing. We note that the processing temperatures in our device fabrication are below 150 °C. This is significantly lower than that of the physical vapor deposition methods (>500 °C) that are typically used in the synthesis of VO_x thin films. These methods are both simple and scalable, paving the way for the creation of flexible IR sensors and truly curved focal plane array detectors for a wide range of sensing and imaging applications. Our work represents

a significant step forward in the field of flexible optoelectronics and opens up exciting new possibilities for the future.

4. Experimental Section

Material Synthesis and Characterization: VO_x nanoparticles were synthesized using a wet chemical process.[44] V_2O_5 powder was reduced using oxalic acid ($C_2H_2O_4.2H_2O$) at a set reflux reaction temperature of 240 °C for 48 h. The reagents were stirred at 450 rpm to an even temperature distribution. The as-synthesized particles filtered and collected from the precipitate were washed in water and dehydrated under vacuum at 550 °C for 90 min. The product was then suspended in IPA/2-butanol solution (volumetric ratio of 9:1) adopting a general ink formulation method,[45] and drop cast for material characterization. A detailed study comparing the synthesis methods and material characteristics of the VO_x nanoparticles compared to those of vapor deposited films, had been reported.[44] TEM images were obtained using a FEI Tecnai F20 microscope at 200 kV. Samples were prepared by drop casting 6 µL of sample suspension on to a 300-mesh copper TEM grid. X-ray diffractograms were collected using a Bruker D8 Advance Powder Diffractometer with a zero-background sample holder equipped with a (Cu- Kα) source. Raman spectroscopy was caried out using a Horiba LabRAM Evolution micro-Raman system equipped with a 532 nm laser, 50 × objective and an 1800 lines mm^{-1} grating. Spectra were obtained at an incident power of 0.25 mW, with a 5 s exposure time and averaged over five measurements. X-ray photoelectron spectroscopy (XPS) was carried out using a Kratos AXIS SUPRA PLUS equipped with a monochromatic Al Kα x-ray source ($h\nu$ = 1486.6 eV). The spectra were collected at 12 kV with an emission current of 10 mA, at a spot size of 700 × 300 μm^2. The infrared photoluminescence (PL) spectrum was measured using a FTIR spectrometer (iS50, Thermo Fisher) equipped with a liquid N_2-cooled HgCdTe detector. The excitation wavelength was 638 nm and the PL was collected with a reflecting objective (15× magnification).[6]

Photodetector Fabrication: IDE patterns (area 0.5 × 0.5 mm^2, electrode width 5 µm, electrode gap 5 µm) were produced via photolithography (MLA150, Heidelberg Instruments, λ = 405 nm) on two types of substrates: 50 µm thick polyimide substrates and polyimide on 300 nm SiO_2/Si substrates. The same fabrication processes were performed on both substrate types. A positive photoresist (AZ1512) was spin-coated on the substrates and, after exposure, AZ726 solution was used to develop the electrode patterns. Chromium (10 nm thick) and gold (100 nm thick) were deposited via electron beam evaporation. The IDEs were obtained after lift-off in acetone. Photodetectors were fabricated by drop casting the particle suspension (10 × 2 µl) onto the IDEs. Devices were annealed under vacuum at 150 °C for 2 h to remove the solvents. Experiments were performed on the photodetectors on polyimide/SiO_2/Si substrates to study the effect of device temperature on detector responsivity. Each chip was packaged in a 28-pin dual in-line chip carrier and heated using a cryostat.

Photodetector Performance Characterization: To study the device performance, a laser that operates in the MWIR spectral range (λ = 2.2 µm) was used that operates in the MWIR spectral range (λ = 2.2 µm). The output of the laser source was coupled to a reflecting objective (magnification 10×) and focused onto the device under characterization. For all measurements, the devices were biased between 100–145 mV using a transimpedance amplifier (TIA, SRS 570) to achieve a fixed dark current (0.2 mA, offset to zero with an input offset) and the photoresponse was obtained using an oscilloscope. Time-resolved photocurrent was obtained by modulating the laser source using a square wave (2 V peak-to-peak, 0.1 Hz). The *I–V* characteristics of the devices were measured using a source measure unit (SMU, Keithley 2450) under dark and illumination conditions (continuous wave operation, 0.26 mW mm^{-2}). The bias dependence of photocurrent and responsivity were determined using data from these measurements. Current noise density was characterized under the same bias conditions using a TIA and a lock-in amplifier (LIA, SRS 860) at θ = 0 ° and θ =100 °. The current noise density spectrum was measured sixteen times and averaged. Photoresponse as a function of power density was characterized using a variable optical density (0.04 – 4) filter wheel that was placed in the beam path. Sixteen photocurrent measurements were performed at each incident power density. These values were averaged. The incident power density on the device was measured through a pinhole aperture (500 µm), by replacing the photodetector with a broadband thermal sensor (Thorlabs, S401C) connected to a power meter (Thorlabs, PM100D).

Visible-SWIR Photoresponsivity Characterization: A laser driven white light source (400–1000 nm) coupled to a monochromator was used for Vis-NIR responsivity characterization. A Xenon lamp coupled to a monochromator (Cornerstone 260i, Newport) was used to characterize the responsivity in the shortwave infrared range (1000–1500 nm). The illumination between 400 to 1500 nm was varied in steps of 10 nm. A long pass filter (750 nm) was used in the beam path for wavelengths ≥ 760 nm as an order sorting filter to remove the second order wavelengths transmitted by the monochromator. A visible objective (λ = 400–1000 nm, magnification 10×) and a visible-NIR objective (λ = 1000–1500 nm, magnification 50×) were used to focus the light onto the device. The photodetectors were biased (145 mV) using a transimpedance amplifier (TIA, SRS 570), with the dark current offset to zero. The light beam was mechanically chopped at 0.1 Hz and the photocurrent was measured with an oscilloscope. The illumination power density at the focal plane was measured through a pinhole aperture (500 µm), using a power meter equipped with calibrated Si (430–750 nm; Thorlabs, S121C) and Ge (750–1500 nm; Thorlabs, S122C) photodiodes. The photoresponsivity was quantified as $R(\lambda) = I_{ph}(\lambda)/P(\lambda)$, where P is the incident power on the device (area 0.5 × 0.5 mm^2). Specific detectivity was calculated as follows:

$$D^* = \frac{R_\lambda \sqrt{A \times \Delta f}}{i_n} \tag{3}$$

where R_λ is the spectral responsivity, A is the detector area in cm^2 and Δf is the bandwidth and i_n noise current measured at 1 Hz.

MWIR-LWIR Photoresponsivity Characterization: MWIR-LWIR photoresponse was characterized using an FTIR spectrometer (Frontier, Perkin Elmer). The black body illumination from the FTIR source was modulated by a Michelson interferometer, which was coupled to a reflecting objective (magnification 40×/10×) and focused onto the photodetector. The photodetectors were biased using the TIA with the dark current offset to zero with an input offset. The amplified photoresponse from the device was then feedback to the external detector interface of the FTIR and Fourier transformed to resolve the wavelength dependent photoresponse ($I_{Ph}(\lambda)$). The relative power spectrum of the blackbody source versus wavelength ($I_{DTGS}(\lambda)$) was measured using the internal deuterated triglycine sulfate (DTGS) detector of the FTIR. The relative infrared photoresponsivity $R(\lambda)$ was calculated as $I_{ph}(\lambda)/I_{DTGS}(\lambda)$ in arbitrary units,[29,43] for the mid-wave to long-wave infrared range. As the modulation frequency of the Michelson interferometer (> 30 Hz) was beyond the frequency bandwidth of the devices, the absolute responsivity at steady state was could not be quantify using this approach. The transmittance and the reflectance of a flexible bolometer was measured under ambient environment, using a microscope (Spotlight, Perkin Elmer) coupled to the FTIR. Air and a gold coated mirror surface were used as references in the tranmittance and reflectance measurements, respectively. Absorbance of the device was calculated as A = (100–T–R)%. Refer to Figure S9 (Supporting Information) for a schematic illustration of the experimental setup.

Temperature Dependent Detector Performance: Photodetectors packaged in a chip carrier were mounted onto a cryostat (Janis Research). Measurements were carried out in ambient pressure, by increasing the chip carrier temperature from 295 to 355 K, in steps of 2 K. *I–V* characteristics were acquired using a source measure unit (Keithley 2450). A laser (λ = 2.2 µm) operated in continuous wave mode was used as the MWIR illumination source. Methods used to vary and measure the incident power density at the focal plane were described in the above "Photodetector performance characterization" section. The detector was biased at 0.4 V using a TIA (SRS, 570) with the dark current offset to zero. Sixteen photocurrent measurements were performed at each incident power density using a LIA

(SRS 860). These values were averaged. Responsivity was calculated as the ratio between the photocurrent and the incident power on the detector.

Tensile Strain Application: Flexible photodetectors were mounted on a home-built strain stage. Electrical contact with the devices was made using a flexible printed circuit (FPC) connector, coupled to a breakout printed circuit board (PCB). Refer to Figure S10 (Supporting Information) for optical images of the photodetectors under strain and Video S1 (Supporting Information) for an animated video of the experiment. The substrate was uniaxially bent by reducing the distance between the FPC end terminals, in steps of 5 mm. Substrate curvature at each step was imaged with a camera. The bend radii and angles were calculated via image processing (ImageJ). MWIR to LWIR range photoresponse was measured using the FTIR under varying bend angles up to 100 °. At each bend angle, 20 spectra were acquired and averaged. These were normalized to the spectrum acquired at $\theta = 0$ °. The endurance of the device over 100 repetitive bend and release cycles was characterized by measuring the photocurrent ($\lambda = 2.2$ µm, 10.7 mW mm^{-2}) at every 10 cycles. These were normalized to the value obtained at the 0th cycle.

Supporting Information

Supporting Information is available from the Wiley Online Library or from the author.

Acknowledgements

S.B. and M.T contributed equally to this work. This work was supported by the Australian Research Council (DP210103428). This work was supported in part by the Australian Research Council (ARC) Centre of Excellence for Transformative Meta-Optical Systems (TMOS, CE200100010) and Centre for Exciton Science (CE170100026). This work was performed in part at the Micro Nano Research Facility (MNRF) at RMIT University in the Victorian Node of the Australian National Fabrication Facility (ANFF). M.T. Acknowledges the support from the Defence Science Institute, an initiative of the State Government of Victoria. The work at Berkeley was funded by the U.S. Department of Energy , Office of Science, Office of Basic Energy Sciences, Materials Sciences and Engineering Division under Contract No. DE-AC02-05-CH11231 (EMAT program KC1201). N.H. acknowledges the support from Postdoctoral Fellowships for Research Abroad of the Japan Society for the Promotion of Science.

Open access publishing facilitated by The University of Melbourne, as part of the Wiley - The University of Melbourne agreement via the Council of Australian University Librarians.

Conflict of Interest

The authors declare no conflict of interest.

Data Availability Statement

The data that support the findings of this study are available from the corresponding author upon reasonable request.

Keywords

bolometers, broadband detectors, flexible photodetectors, infrared detectors, vanadium dioxide

Received: February 15, 2023
Revised: May 22, 2023
Published online: June 21, 2023

[1] X. Chen, K. Shehzad, L. Gao, M. Long, H. Guo, S. Qin, X. Wang, F. Wang, Y. Shi, W. Hu, Y. Xu, X. Wang, *Adv. Mater.* **2020**, *32*, 1902039.
[2] S.-I. Park, A.-P. Le, J. Wu, Y. Huang, X. Li, J. A. Rogers, *Adv. Mater.* **2010**, *22*, 3062.
[3] C. Wu, D. Wang, Y. Zhang, F. Gu, G. Liu, N. Zhu, W. Luo, D. Han, X. Guo, B. Qu, S. Wang, Z. Bian, Z. Chen, L. Xiao, *Adv. Funct. Mater.* **2019**, *29*, 1902974.
[4] I. Jung, J. Xiao, V. Malyarchuk, C. Lu, M. Li, Z. Liu, J. Yoon, Y. Huang, J. A. Rogers, *Proc. Natl. Acad. Sci. USA* **2011**, *108*, 1788.
[5] J. S. Price, X. Sheng, B. M. Meulblok, J. A. Rogers, N. C. Giebink, *Nat. Commun.* **2015**, *6*, 6223.
[6] S.-B. Rim, P. B. Catrysse, R. Dinyari, K. Huang, P. Peumans, *Opt. Express* **2008**, *16*, 4965.
[7] H. C. Ko, M. P. Stoykovich, J. Song, V. Malyarchuk, W. M. Choi, C.-J. Yu, J. B. Geddes Iii, J. Xiao, S. Wang, Y. Huang, J. A. Rogers, *Nature* **2008**, *454*, 748.
[8] L. Gu, S. Poddar, Y. Lin, Z. Long, D. Zhang, Q. Zhang, L. Shu, X. Qiu, M. Kam, A. Javey, Z. Fan, *Nature* **2020**, *581*, 278.
[9] Y. M. Song, Y. Xie, V. Malyarchuk, J. Xiao, I. Jung, K.-J. Choi, Z. Liu, H. Park, C. Lu, R.-H. Kim, R. Li, K. B. Crozier, Y. Huang, J. A. Rogers, *Nature* **2013**, *497*, 95.
[10] B. Dai, L. Zhang, C. Zhao, H. Bachman, R. Becker, J. Mai, Z. Jiao, W. Li, L. Zheng, X. Wan, T. J. Huang, S. Zhuang, D. Zhang, *Nat. Commun.* **2021**, *12*, 6458.
[11] K.-H. Jeong, J. Kim, L. P. Lee, *Science* **2006**, *312*, 557.
[12] L. Li, A. Y. Yi, *Opt. Express* **2010**, *18*, 18125.
[13] S. Thiele, K. Arzenbacher, T. Gissibl, H. Giessen, A. M. Herkommer, *Sci. Adv.* **2017**, *3*, 1602655.
[14] Z.-Y. Hu, Y.-L. Zhang, C. Pan, J.-Y. Dou, Z.-Z. Li, Z.-N. Tian, J.-W. Mao, Q.-D. Chen, H.-B. Sun, *Nat. Commun.* **2022**, *13*, 5634.
[15] M. E. Itkis, F. Borondics, A. Yu, R. C. Haddon, *Science* **2006**, *312*, 413.
[16] F. H. L. Koppens, T. Mueller, P. Avouris, A. C. Ferrari, M. S. Vitiello, M. Polini, *Nat. Nanotechnol.* **2014**, *9*, 780.
[17] X. Wang, H. Liu, J. Wu, J. Lin, W. He, H. Wang, X. Shi, K. Suenaga, L. Xie, *Adv. Mater.* **2018**, *30*, 1800074.
[18] L. Zeng, D. Wu, J. Jie, X. Ren, X. Hu, S. P. Lau, Y. Chai, Y. H. Tsang, *Adv. Mater.* **2020**, *32*, 2004412.
[19] W. Su, S. Zhang, C. Liu, Q. Tian, X. Liu, K. Li, Y. Lv, L. Liao, X. Zou, *Nano Lett.* **2022**, *22*, 10192.
[20] M. Z. Nawaz, L. Xu, X. Zhou, J. Li, K. H. Shah, J. Wang, B. Wu, C. Wang, *ACS Appl. Mater. Interfaces* **2022**, *14*, 19659.
[21] T. Zhu, Y. Yang, L. Zheng, L. Liu, M. L. Becker, X. Gong, *Adv. Funct. Mater.* **2020**, *30*, 1909487.
[22] C. Xie, F. Yan, *Small* **2017**, *13*, 1701822.
[23] M. Freitag, T. Low, F. Xia, P. Avouris, *Nat. Photonics* **2013**, *7*, 53.
[24] J. Yan, M. H. Kim, J. A. Elle, A. B. Sushkov, G. S. Jenkins, H. M. Milchberg, M. S. Fuhrer, H. D. Drew, *Nat. Nanotechnol.* **2012**, *7*, 472.
[25] Z. Sun, Z. Liu, J. Li, G.-a. Tai, S.-P. Lau, F. Yan, *Adv. Mater.* **2012**, *24*, 5878.
[26] C. Li, C.-J. Han, G. Skidmore, *Opt. Eng.* **2011**, *50*, 061017.
[27] A. Håkansson, M. Shahi, J. W. Brill, S. Fabiano, X. Crispin, *Adv. Electron. Mater.* **2019**, *5*, 1800975.
[28] A. Yaradanakul, D. P. Butler, Z. Celik-Butler, *IEEE Trans. Electron Devices* **2002**, *49*, 930.
[29] S. Balendhran, Z. Hussain, V. R. Shrestha, J. Cadusch, M. Ye, N. Sefidmooye Azar, H. Kim, R. Ramanathan, J. Bullock, A. Javey, V. Bansal, K. B. Crozier, *ACS Appl. Mater. Interfaces* **2021**, *13*, 38544.
[30] R. Pfattner, V. Lebedev, E. Laukhina, S. C. Kumar, A. Esteban-Martin, V. Ramaiah-Badarla, M. Ebrahim-Zadeh, F. P. G. de Arquer, G. Konstantatos, V. Laukhin, C. Rovira, J. Veciana, *Adv. Electron. Mater.* **2015**, *1*, 1500090.
[31] J. A. Creeden, S. E. Madaras, D. B. Beringer, M. R. Beebe, I. Novikova, R. A. Lukaszew, *Sci. Rep.* **2019**, *9*, 9362.

[32] S. Lee, I. N. Ivanov, J. K. Keum, H. N. Lee, *Sci. Rep.* **2016**, *6*, 19621.
[33] T. Paik, S.-H. Hong, E. A. Gaulding, H. Caglayan, T. R. Gordon, N. Engheta, C. R. Kagan, C. B. Murray, *ACS Nano* **2014**, *8*, 797.
[34] Q. Song, W. Gong, G. Ning, H. Mehdi, G. Zhang, J. Ye, Y. Lin, *Phys. Chem. Chem. Phys.* **2014**, *16*, 8783.
[35] Y. Ji, Y. Zhang, M. Gao, Z. Yuan, Y. Xia, C. Jin, B. Tao, C. Chen, Q. Jia, Y. Lin, *Sci. Rep.* **2014**, *4*, 4854.
[36] S. Lee, T. L. Meyer, C. Sohn, D. Lee, J. Nichols, D. Lee, S. S. A. Seo, J. W. Freeland, T. W. Noh, H. N. Lee, *APL Mater.* **2015**, *3*, 126109.
[37] M. M. Qazilbash, M. Brehm, B.-G. Chae, P.-C. Ho, G. O. Andreev, B.-J. Kim, S. J. Yun, A. V. Balatsky, M. B. Maple, F. Keilmann, H.-T. Kim, D. N. Basov, *Science* **2007**, *318*, 1750.
[38] N. Fieldhouse, S. M. Pursel, M. W. Horn, S. S. N. Bharadwaja, *J. Phys. D Appl. Phys.* **2009**, *42*, 055408.
[39] R. T. R. kumar, B. Karunagaran, D. Mangalaraj, K. N. Sa, P. Manoravi, M. Joseph, G. Vishnu, *Smart Mater. Struct.* **2003**, *12*, 188.
[40] S. Chen, M. Lust, N. Ghalichechian, *Microsyst. Technol.* **2021**, *27*, 2815.
[41] Y.-Y. Su, X.-W. Cheng, J.-B. Li, Y.-K. Dou, F. Rehman, D.-Z. Su, H.-B. Jin, *Appl. Surf. Sci.* **2015**, *357*, 887.
[42] T. Uchida, A. Matsushita, T. Tachiki, *Jpn. J. Appl. Phys.* **2014**, *53*, 068009.
[43] H. Kim, S. Z. Uddin, D.-H. Lien, M. Yeh, N. S. Azar, S. Balendhran, T. Kim, N. Gupta, Y. Rho, C. P. Grigoropoulos, K. B. Crozier, A. Javey, *Nature* **2021**, *596*, 232.
[44] M. Taha, S. Balendhran, P. C. Sherrell, N. Kirkwood, D. Wen, S. Wang, J. Meng, J. Bullock, K. B. Crozier, L. Sciacca, *J. Mater. Chem. A* **2023**, *11*, 7629.
[45] G. Hu, L. Yang, Z. Yang, Y. Wang, X. Jin, J. Dai, Q. Wu, S. Liu, X. Zhu, X. Wang, T.-C. Wu, R. C. T. Howe, T. Albrow-Owen, L. W. T. Ng, Q. Yang, L. G. Occhipinti, R. I. Woodward, E. J. R. Kelleher, Z. Sun, X. Huang, M. Zhang, C. D. Bain, T. Hasan, *Sci. Adv.* **2020**, *6*, eaba5029.